

# Shear velocity structure of crust and uppermost mantle in China from surface wave tomography using ambient noise and earthquake data

Zhen J. Xu · Xiaodong Song · Sihua Zheng

Received: 28 April 2013 / Accepted: 26 August 2013 / Published online: 25 December 2013

© The Seismological Society of China, Institute of Geophysics, China Earthquake Administration, and Springer-Verlag Berlin Heidelberg 2013

**Abstract** We present a 3D model of shear velocity of crust and upper mantle in China and surrounding regions from surface wave tomography. We combine dispersion measurements from ambient noise correlation and traditional earthquake data. The stations include the China National Seismic Network, global networks, and all the available PASSCAL stations in the region over the years. The combined data sets provide excellent data coverage of the region for surface wave measurements from 8 to 120 s, which are used to invert for 3D shear wave velocity structure of the crust and upper mantle down to about 150 km. We also derive new models of the study region for crustal thickness and averaged  $S$  velocities for upper, mid, and lower crust and the uppermost mantle. The models provide a fundamental data set for understanding continental dynamics and evolution. The tomography results reveal significant features of crust and upper mantle structure, including major basins, Moho depth variation, mantle velocity contrast between eastern and western North China Craton, widespread low-velocity zone in mid-crust in much of the Tibetan Plateau, and clear velocity contrasts of the mantle lithosphere between north and southern Tibet with significant  $E$ – $W$  variations. The low

velocity structure in the upper mantle under north and eastern TP correlates with surface geological boundaries. A patch of high velocity anomaly is found under the eastern part of the TP, which may indicate intact mantle lithosphere. Mantle lithosphere shows striking systematic change from the western to eastern North China Craton. The Tanlu Fault appears to be a major lithosphere boundary.

**Keywords** Surface wave tomography · China · Ambient noise · Tibetan Plateau · North China Craton

## 1 Introduction

Located in the southeastern portion of the Eurasian plate, China and its surrounding regions are highly geologically heterogeneous. Its present diverse structures and tectonics are controlled by the interactions of the Eurasian plate, the Indian plate, the Pacific plate, and the Philippine plate. In the southeast, the India–Eurasia collision about 60 Ma leads to significant crustal shortening and the rising of the broad Tibetan Plateau (TP) with an average elevation of 5,000 m, and the world's highest mountain range, the Himalaya. In the east, the Pacific plate and the Philippine plate subduct underneath the Eurasian plate, forming the western Pacific island arcs, and marginal seas. These aforementioned ongoing tectonics result in dramatic complexities in surface topography and crustal and mantle deformation, as well as intensive seismic and volcanic activities. Ancient platforms, deep sediment basins and high plateaus are all present in this region, separated by fault zones, sutures, or mountain belts (Fig. 1). China and its surrounding regions have constantly drawn the attention of geologists and geophysicists for decades, due to its

---

Z. J. Xu · X. Song  
Department of Geology, University of Illinois, Urbana,  
IL 61801, USA

X. Song (✉)  
Institute of Geophysics and Geodynamics, School of Earth  
Sciences and Engineering, Nanjing University, Nanjing 210093,  
China  
e-mail: xiao.d.song@gmail.com

S. Zheng  
Institute of Earthquake Science, China Earthquake  
Administration, Beijing 10036, China

complex geology and many fundamental questions, e.g., the shortening and extension of the TP, the rejuvenation of North China block, and the deep subducted crust in the Dabie Mountain, to name a few. Investigations of 3D crustal and mantle velocity structure of this region are important for better understanding such tectonic features and processes, which also have important implications for earthquake hazards and oil and mineral resources.

Seismic tomography is an effective tool to study the heterogeneity of the earth's interior. Many research groups have conducted body wave and surface wave tomography studies of China and its surrounding regions using regional and distant earthquake data (e.g., Ritzwoller et al. 1998; Xu et al. 2002; Huang and Zhao 2006; Liang et al. 2004; Li et al. 2008; Obrebski et al. 2012). However, these earthquake-based studies have their own limitations, in that earthquake distributions are usually uneven, leading to nonuniform ray path coverage with some areas poorly illuminated. The resolution of tomographic results can also be affected by errors in earthquake location and origin time.

The recent revolutionary method of surface wave tomography based on the retrieval of the empirical Green's function (EGF) from ambient noise (e.g., Weaver and Lobkis 2001, 2004; Campillo and Paul 2003; Shapiro and Campillo 2004) has provided additional data coverage with unique advantages. First of all, EGFs are retrieved between station pairs, thus the ray coverage depends on station distribution, which is in general more uniform than earthquake distribution. Secondly, uncertainties in earthquake source are eliminated. Moreover, short period surface waves, which are difficult to extract using conventional earthquake data due to earthquake source spectrum, attenuation, and scattering, can be more easily retrieved using this method, thus providing better constraint on shallow structure, especially the crustal structures. This new type of data has been quickly applied to different

tomography studies (e.g., Shapiro et al. 2005; Sabra et al. 2005; Yao et al. 2006, 2008; Yang et al. 2007, 2012; Bensen et al. 2008; Lin et al. 2008; Zheng et al. 2008, 2011; Sun et al. 2010; Zhou et al. 2012). One drawback of this method, however, is that longer periods of surface wave signals (>70 s) are usually weak and unstable. On the other hand, surface waves from earthquakes contain stable signals at a longer period range. Therefore, combining both ambient noise correlation data and earthquake data provides a broad period range that puts stronger constraint and improves resolution on shallow to deep structures. In the recent studies, Yao et al. (2008) and Yang et al. (2008) performed surface wave tomography using combined ambient noise and earthquake data in Southeast Tibet and South Africa, respectively.

In this study, we present a 3D shear wave velocity model of China and surrounding regions using Rayleigh dispersion measurements from both ambient noise correlation and earthquake data. Below we describe the data the method, present our 3D shear-wave velocity model as well as a derived crustal and uppermost mantle model, and discuss some important features of the model (in particular, the TP and North China regions).

## 2 Data and method

### 2.1 Data

The data we used can be divided into two categories: the EGFs from ambient noise correlation and the traditional earthquake data. Part of the ambient noise data have been used in the previous studies by Zheng et al. (2008) and Sun et al. (2010). For this study, we included more stations and much longer time periods to increase inter-station coverage. We acquired 18-month continuous data in vertical component from new Chinese National Seismic Network (CNSN) in the time period from November 2003 to October 2004 and from January 2007 to June 2007. The CNSN includes 48 broadband digital permanent stations

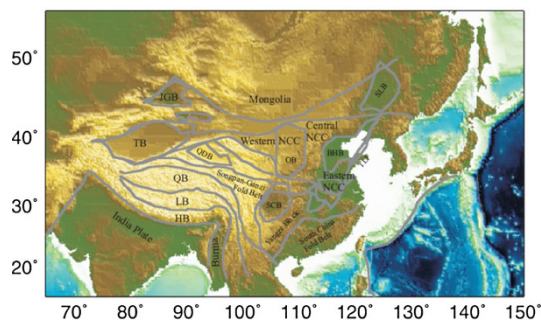


**Fig. 1** A tectonic map of China. Gray thick lines indicate major geological unit boundaries. JGB Junggar Basin, TB Tarim Basin, QDB Qaidam Basin, QB Qiangtang block, LB Lhasa Block, HB Himalaya Block, SCB Sichuan Basin, OB Ordos Basin, NCC North China Craton, SLB Songliao Basin, BHB Bohai Bay, TLF Tanlu Fault

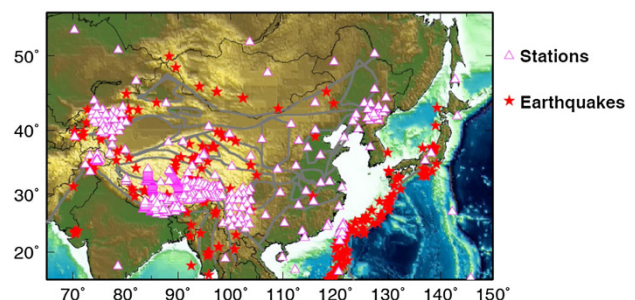


**Fig. 2** Distributions of seismic stations (triangles) and earthquakes (stars) used in this study

distributed relatively uniformly across the Chinese continent since year 2000. We also downloaded vertical component of all the available continuous broadband and long period data in our study region in the time period from January 1991 to June 2007 from permanent global and regional network stations as well as temporary PASSCAL stations from the IRIS DMC. The total number of stations included in our study is 528 (Fig. 2).

For the earthquake data set, we gathered the available event data for all the stations from 155 earthquakes in our study region with depth shallower than 40 km and magnitude larger than 5.5 in the preliminary determination of epicenters (PDE) catalog from 2000 to 2007. We also included event data recorded by CNSN stations for additional 197 earthquakes with magnitude from 5.0 to 5.5 in the PDE catalog in the same depth range and time period (Fig. 2).

## 2.2 Method

All the broadband continuous data are downsampled to 1 sample per second (sps) to ensure the consistency in sampling rate with long-period data. The procedures we used to retrieve EGFs are described in great details in Bensen et al. (2007) and are summarized in our previous studies (Zheng et al. 2008; Sun et al. 2010). The continuous data are bandpass filtered from 5 to 150 s. The signal-to-noise ratio (SNR) of the selected EGFs is greater than 10. Group and phase velocity dispersion curves from 8 to 70 s are measured using frequency–time analysis (FTAN) (Levshin and Ritzwoller 2001). The numbers of group and phase velocity measurements are very similar at all periods. The detailed method of measuring group and phase velocity dispersions is discussed in Bensen et al. (2007) and has been used by Lin et al. (2008) for the western US and by Zheng et al. (2008) and Sun et al. (2010) for surface wave tomography in China. Group velocity dispersion curves of earthquake data are measured in the same way for periods from 8 to 120 s. However, we exclude the phase velocity measurement of earthquake data to avoid the uncertainty of initial phase. The incorporated data set has maximum of ~35,000 measurements for group velocity and ~22,500 measurements for phase velocity at period of 20 s (Fig. 3), more than quadruple our previous measurements (Sun et al. 2010). For periods from 8 to 70 s, the combined group and phase velocity measurements from ambient noise correlations are about 2–4 times the group velocity measurements from earthquake data.

Our shear wave velocity tomography is performed in a two-step procedure. First, we use the dispersion measurements to construct phase and group velocity maps at different period (8–70 s for phase velocity and 8–120 s for

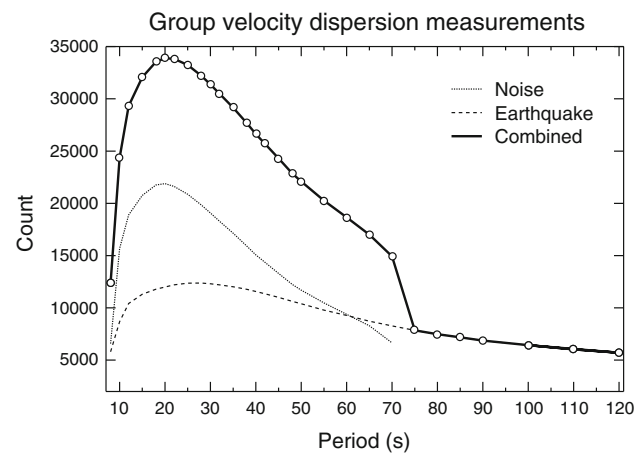


**Fig. 3** Numbers of Rayleigh group dispersion measurements for different periods from ambient noise correlations, earthquake data, and the combination of both ambient noise and earthquake data. The *open circles* indicate the periods at which the group and phase velocities are measured. Both group and phase velocities are measured from EGFs from ambient noise correlations for periods up to 70 s. The curve for the numbers of the phase velocity dispersion measurements (not shown) is very similar to that of the group velocity measurements. For earthquake data, only group velocities are measured (up to 120 s)

group velocity). This is done with a linearized inversion by minimizing the following quantity:

$$\min(\|Am - r\|^2 + \lambda^2 \|m\|^2 + \varphi^2 \|Lm\|^2)$$

The first term is data misfit, in which  $m$  is the parameter vector,  $A$  is the coefficient matrix,  $r$  is the vector of travel time residuals. The second term is the model regularization with a damping parameter of non-zero real number  $\lambda$ . The third term is the smoothing constraint with non-zero real number  $\varphi$ . The smoothing operator  $L$  is the Laplacian operator (Lees and Crosson 1989). A larger  $\lambda$  value yields smaller velocity perturbations and the result is closer to the initial model. A larger  $\varphi$  value results in a smoother image. The choice of  $\lambda$  and  $\varphi$  is quite empirical. We experimented different pairs of  $\lambda$  and  $\varphi$  and choose the ones that balance the data misfit, model damping, and smoothness. Since our data set contains a large amount of measurements involving over 500 stations and 300 events, bad quality data still possibly exist in the data set, even though the data used have been selected according to SNR. Therefore, it is necessary to apply additional data filtering. We select a subset of the data excluding event data and some dense temporary PASSCAL arrays, such as the HICLIMB data, and perform group and phase velocity inversions. The reason we exclude event data is that we would like to exclude the uncertainties in the event data such as mislocations and only use the high quality ambient noise data as our starting data set for data cleaning. Then we use inverted velocity dispersion models as filters and clean the

whole data set. For each measurement in each period, we use the inverted model to calculate the theoretical travel time. We then calculate the mean and standard deviation of all the travel-time residuals and all relative residuals (in percentage relative to the observed travel time). We then exclude the measurements with either residual or relative residual outside two standard deviations from the corresponding mean value. The reason we also consider relative residual is that relative residual is less affected by distance. After the whole data set is cleaned, we perform a new inversion, which includes both ambient noise and event data and use the updated model to clean the whole data set once more. Since good quality event data are included in the inversion after first cleaning, we are able to better select the high quality data, particularly at long periods. The data set that is cleaned twice becomes our final data set. We examine the images between first, second clean and the final results and find they are indeed very similar. The final group and phase velocity maps are then constructed using the final data set. The grid size is  $1^\circ \times 1^\circ$ .

The second step of our shear wave tomography involves the inversion of 1D shear wave velocity for each node as a function of depth from the inverted group and phase velocity dispersions [using the computer program by Herrmann (1991)]. A 3D velocity model is then constructed through linear interpolations between nodes. The model is divided into 25 layers with thickness of 5 km at the top 50, 10 km down to the depth of 150 km, and greater thickness below that. The initial model is a 1D homogeneous model with a constant velocity. Only shear wave velocity is inverted since Rayleigh wave is mostly sensitive to shear velocity.

### 2.3 Resolution test

To test the resolution of our inversion, we perform a checkerboard test. The input model consists of  $3^\circ$  by  $3^\circ$  alternating positive and negative pattern with 5 % velocity perturbation. From shear wave model, we calculate group and phase velocity at each node for the periods we used in real inversion. We then calculate group and phase dispersion curves using exact the ray path as in real inversion. A random noise with a 5-s standard deviation is added to the calculated travel time. Shear wave velocities are then inverted using the two-step inversion as described in the last section (Fig. 4). The checkerboard pattern is generally well recovered for the top 150 km in most part of the Chinese continent, even though the resolution gradually deteriorates at deeper depth. The best resolution appears in the southwestern China, i.e., the TP and its surrounding regions, due to the densest ray coverage from different PASSCAL experiments and active seismicity.

## 3 Results

Our 3D shear wave velocity results show remarkable features that correlate with surface geology and regional tectonic settings (Fig. 5). At shallow depth (7.5 km), low velocity structures correspond to major sediment basins (e.g., Jungar, Tarim, Qaidam, Ordos, Sichuan, Songliao, North China). Low velocity also appears at Himalaya collision front, Central to Northern Tibet, Pacific island arcs and marginal seas. Yangtze Craton and Korean peninsula, on the other hand, show prominent high as a velocity block at shallow depth.

At depth around 30 km, the most prominent feature is the velocity contrast between the eastern and the western China, in which the western China, with high elevations, shows low velocities, suggesting a thickened crust, while the eastern China shows high velocities because of a thinner crust. Of particular interest at this depth range is the extremely low velocity (with a decrease of up to 15 %) widespread in the whole TP, which is referred as mid crust low velocity zone possibly due to weak and mobile mid crust.

At depth of 55 km, the TP and Songpan-Ganzi Fold Belt still show prominent low velocities. However, all the major basins in western China (Tarim, Junggar, Qaidam, Ordos, and Sichuan) start to show high velocities, suggesting these basins are tectonically stable with little deformation. At 75 km (which in the mantle for most regions except some parts of the TP), the TP, and Songpan-ganzi Fold Belt is in low velocities but velocity in northern Tibet is even lower. Himalaya collision front shows as a high velocity block, indicating a cold and rigid Indian plate. High velocity is even clearer in the basins surrounding the TP (Tarim, Ordos, Qaidam, Tulufan, and Sichuan), indicating they are isolated solid blocks that confine the deformation of the TP. These basins have deep roots with high velocity features extended to a depth at least 150 km. The Pacific island arcs are in low velocity, which may indicate hot material at 75 km depth.

At 95 km, most part of the eastern China now features low velocity structure, which may indicate a thin lithosphere. Low velocity also appears in northern Tibet, Songpan-Ganzi, and Yunnan region. These low velocity structures indicate hot and highly deformed Asian mantle lithosphere and possible existence of partial melt. High velocity appears in major basins in the west, the Himalaya collision front and southern Tibet. The high velocity in the southern Tibet, ceased at Bangong-Nujiang suture, may indicate the rigid Indian lithosphere. Therefore, Bangong-Nujiang suture may be the boundary where the underplating Indian mantle lithosphere detaches from Asian mantle lithosphere and sinks into the deeper mantle. This low velocity features are clearer at 115 and 145 km. However, there is also a high velocity structure from about  $92^\circ$  to

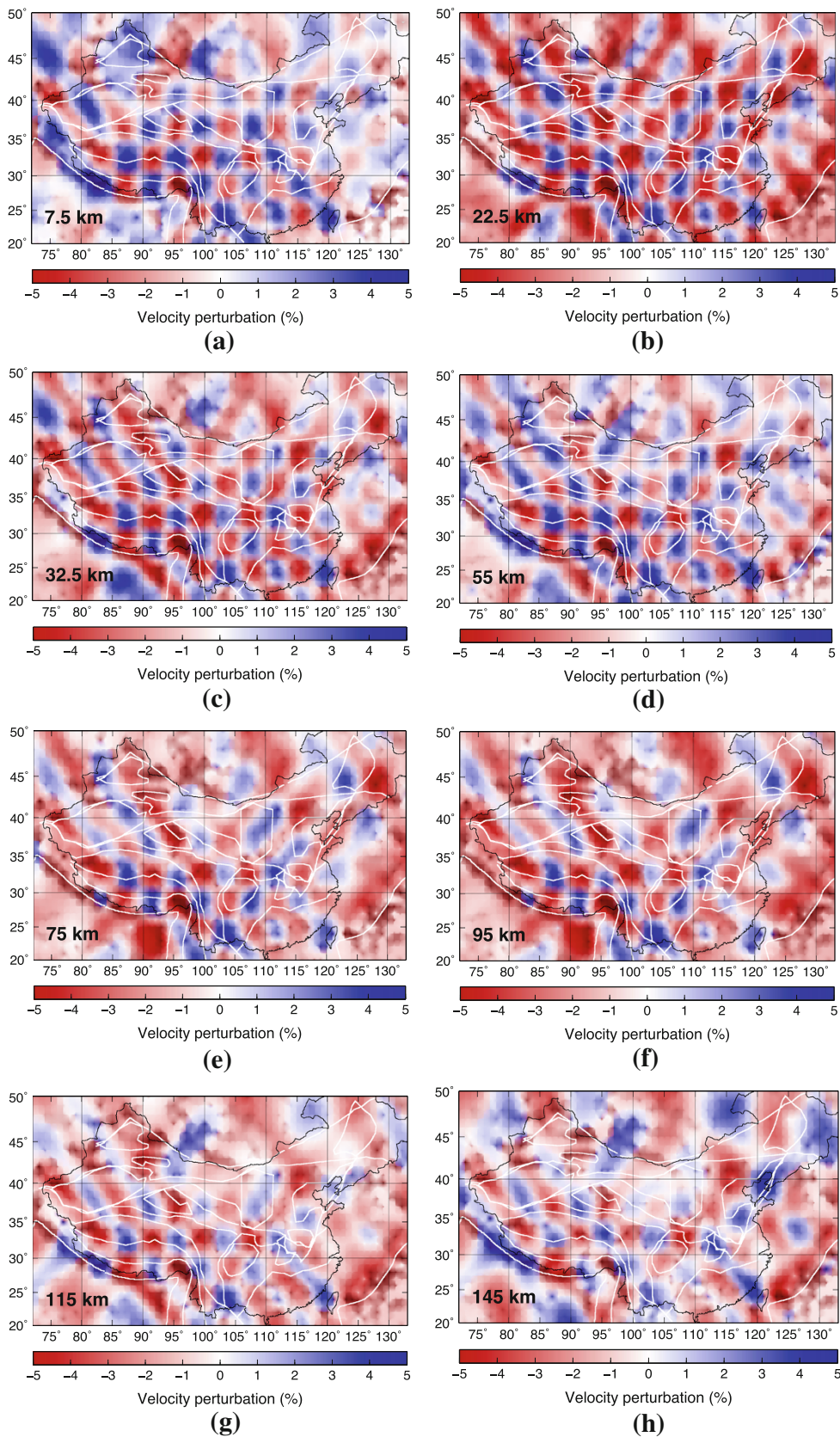


**Fig. 4** Results of checkerboard tests at various depths. The input is alternating pattern of  $3^\circ \times 3^\circ$  with velocity perturbation of 5 %. A random noise with 5-s standard deviation is added to the synthetic data

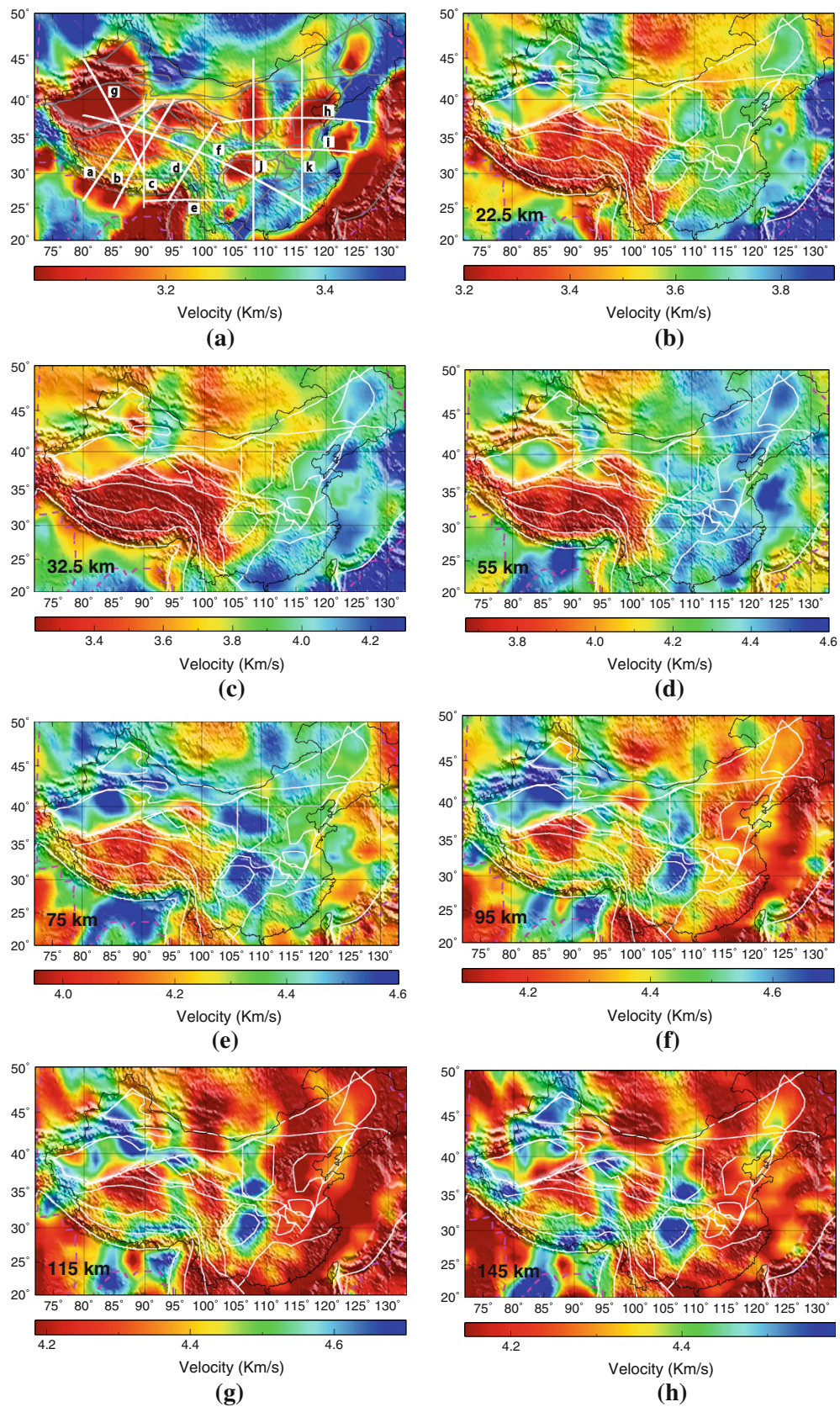


**Fig. 5**  $S$  velocity maps at different depths from our inverted model. White great circle paths in **a** indicate the cross sections shown in Fig. 6

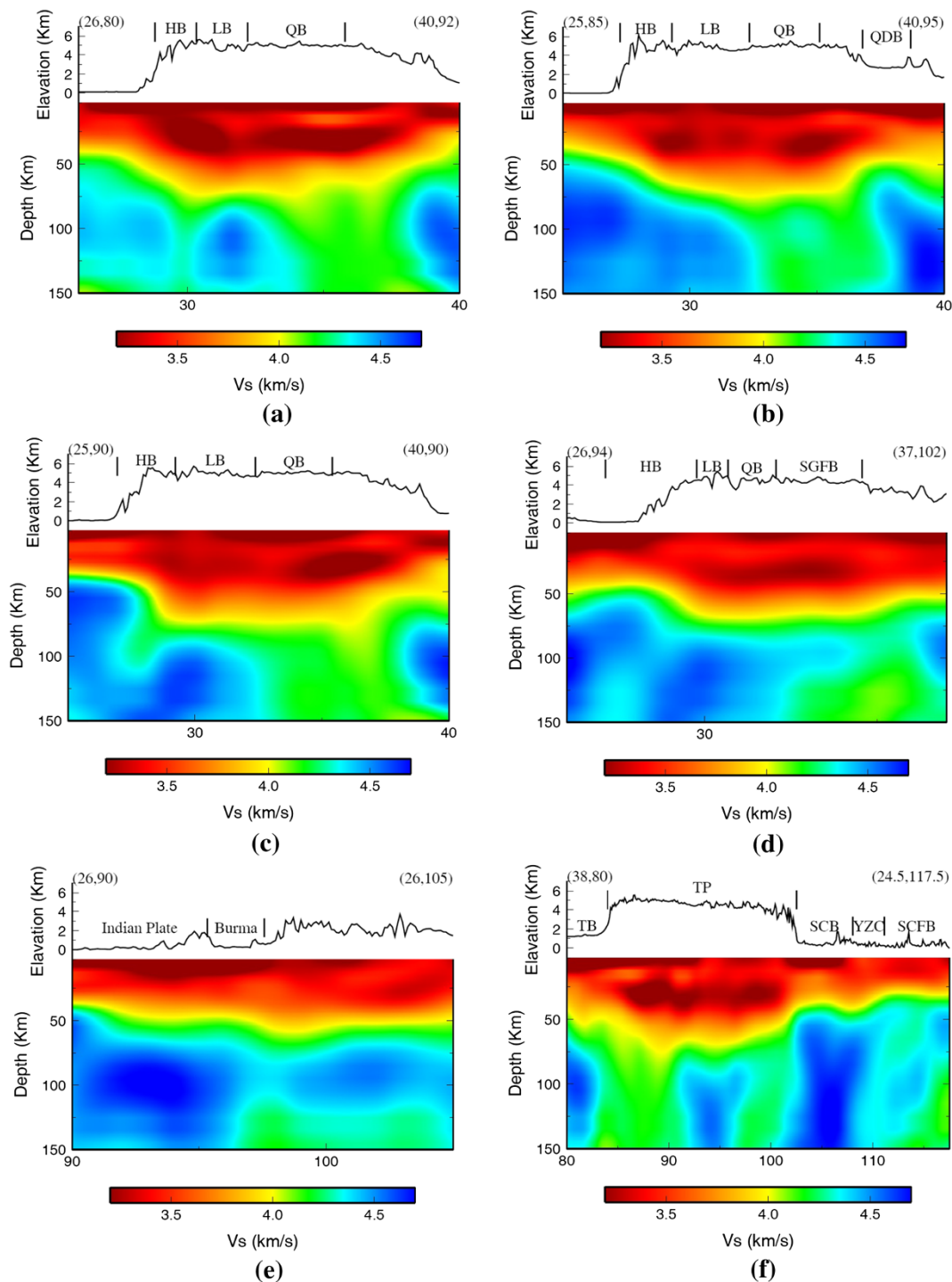


**Fig. 6** S velocity cross-sections of our model. **a–k** correspond to the cross sections along great circle paths labeled in Fig. 5a

98°E in the eastern Tibet. This feature also found in Pn model (Liang and Song 2006) and Rayleigh wave tomography (Huang et al. 2003).

These features can be viewed along a few representative profiles (Fig. 6). In particular, Fig. 6f is a cross section passing through many interesting geological units, including Tarim basin, northern Tibet, Sichuan basin, Yangze

Craton and South China fold belt. Several striking features are shown in this profile, Tarim basin and Sichuan basin show slow velocity of sediment deposition at shallow depth and fast velocity in the mantle to a depth at least to 150 km. Mid crust low velocity zone appears under the TP. Low mantle lithosphere under northwestern TP and high velocity structure in the eastern TP are clearly shown in the

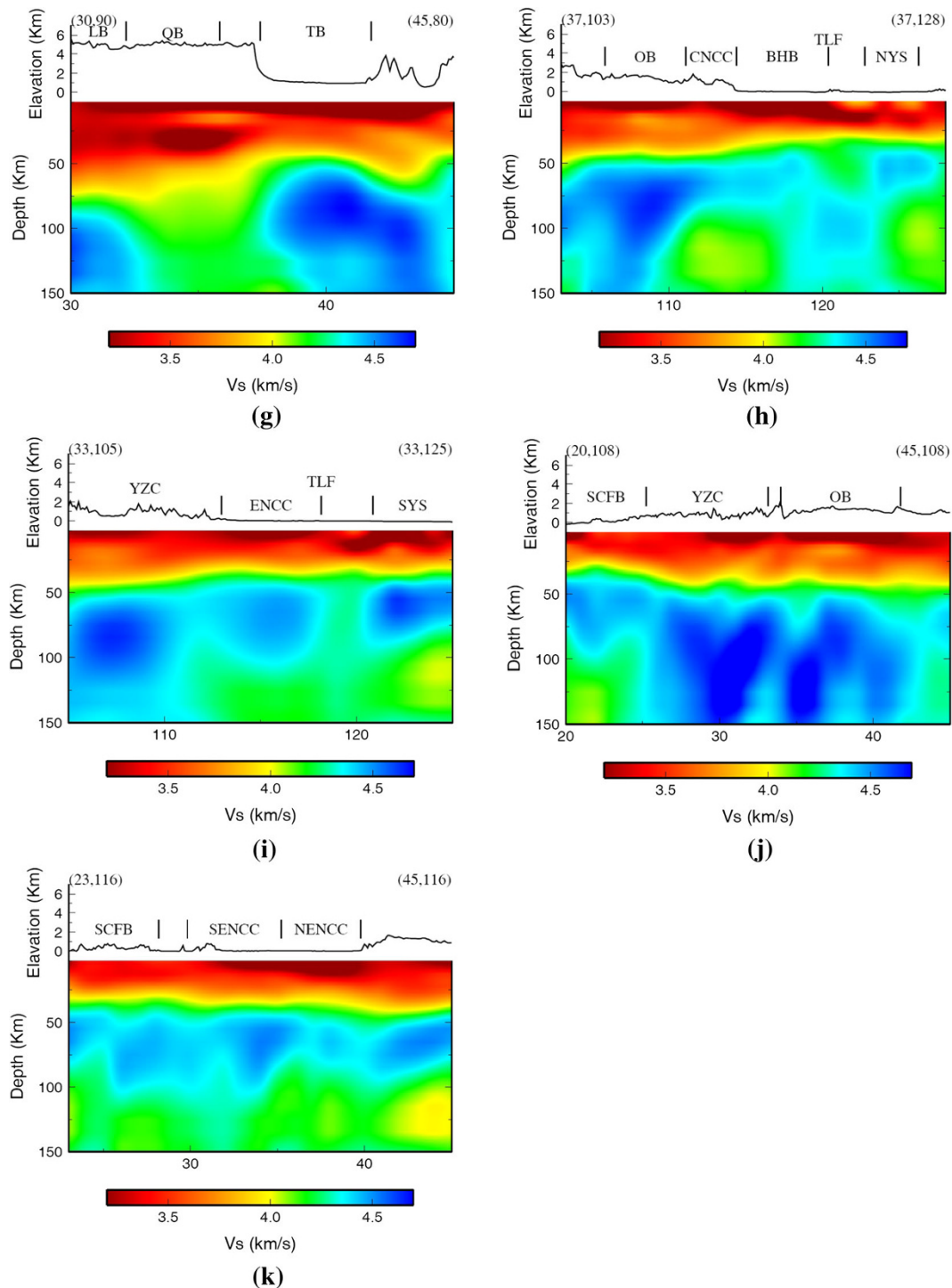


**Fig. 6** continued

cross section. Yangze Craton also shows thick continent root with high mantle velocity extended to larger than 150 km. Crust thickness and lithosphere is thinner under South China fold belt. Low velocity below lithosphere at depth around 80 km under South China Fold Belt indicates the present of hot and soft asthenosphere materials, possibly caused by the removal of continent root.

## 4 Discussion

### 4.1 Comparing group velocity model with earthquake data only

Since earthquake data account for about 50 % of total group velocity measurements from 8 to 70 s (or about a quarter of



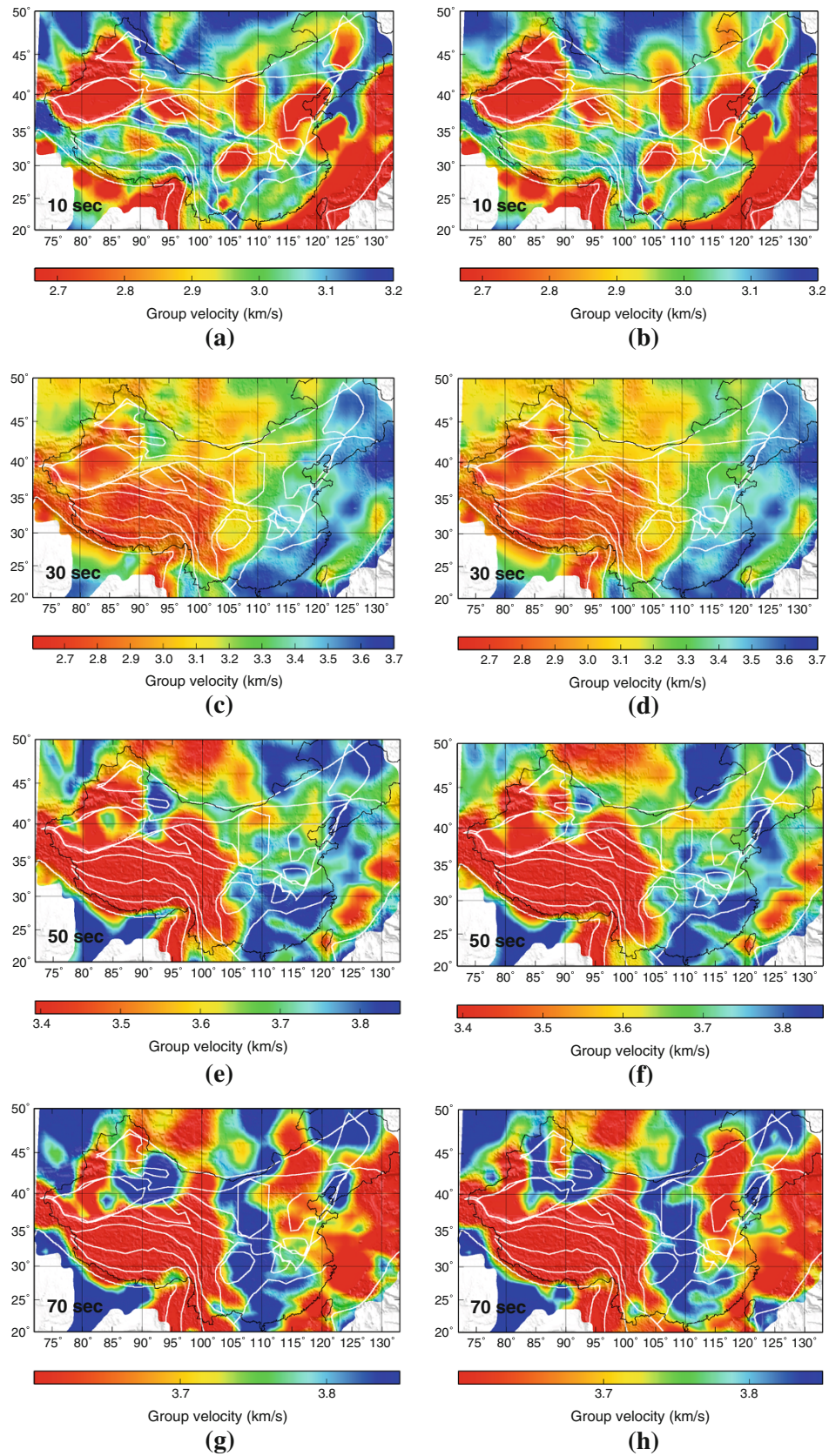


**Fig. 7** Comparison of group velocity maps at 10, 30, 50, 70 s, using the combined data set (*left panels*) and the earthquake data only (*right panels*)

the group and phase velocity measurements), it is useful to compare earthquake data with ambient noise data to examine their compatibility. We perform group velocity inversion with earthquake data only and compare the results to the images using the whole data set. The results from two data sets are generally consistent (Fig. 7). Furthermore, comparing to the results by Sun et al. (2010) using ambient noise data only, we find general similarities, suggesting the consistency of the earthquake data and the ambient noise data. Most major features are similar, e.g., low velocity in sediment basins at short periods, low velocity zones throughout most of the TP, and the eastern-western velocity contrast at intermediate periods, although there are some differences in details. Therefore, we conclude that earthquake data and EGFs provide complimentary group velocity measurements for surface wave tomography.

#### 4.2 Tibetan Plateau

We have outlined above some important features of our model. Here we examine further some detailed features of the TP, a region of particular interest because of its active tectonics and mountain building processes. Figure 6a–d shows a few profiles across the TP (the locations of the cross sections are shown in Fig. 5a). Crust is much thickened under the high Plateau as evidenced from the crustal velocity contours. Prominent low velocity zones in the mid crust underneath the most of the TP appear in all these profiles. Mantle high velocity structure extends only to southern TP and ceases at Bangong-Nujiang suture. This high velocity structure indicates the underplating Indian mantle lithosphere, which is detached from Asian mantle lithosphere in northern TP, leaving hot, highly deformed, and possible partial molten Asian mantle lithosphere. Contrasts in upper mantle *P* and *S* velocities between southern and northern TP are well documented even in early studies of the region (e.g., Chen and Molnar 1981; Holt and Wallace 1990; Rodgers and Schwartz 1998). The northwestern TP has pronounced low velocities from the crust to the mantle, indicating the mantle source of the Cenozoic volcanism of Qiangtang terrain. Our images reveal that the mantle low velocity structure under northwestern TP extends eastward to Songpan-Ganzi fold belt in the north TP then turns south beneath eastern TP and further south to Indo-China, which is consistent with observed *P<sub>n</sub>* velocity anomalies at the uppermost mantle (Liang and Song 2006). The consistency between geological boundaries on surface and sharp velocity contrast boundaries in uppermost mantle may suggest strong deformation coupling between crust and, at least uppermost mantle, if not whole lithosphere. The reason of the high velocity structure in the eastern TP (Figs. 5g, h, 6f) is not well understood. Geochronology study by Chung et al.

(1998) suggests that the lower lithosphere under eastern TP, where the high velocity mantle structure is imaged, is removed 40 million years ago, inducing rapid uplift of the TP and magma activities. While in western TP, the removal of lower lithosphere started only 20 million years ago. The velocity contrast between eastern and western TP seems correlate with the observation of geochronology study. If the high velocity structure indicates an early lithosphere, it would mean that the piece of lithosphere was not detached and remains in the upper mantle. Figure 6e shows an east–west profile across Himalaya collision front and southeastern margin of the TP. Cross section reveals relative thick low velocity features at top 15–20 km under India plate and Burma with thickened fast mantle lithosphere, suggesting Indian lithosphere may deeply subduct into deeper mantle under Burma as imaged by Li et al. (2008). Figure 6g shows a profile across Tibet, Tarim basin, and Tien-Shan Mountain. Like other profiles, the crust is thickened under Tibet and Tien-Shan Mountain. High velocity appears under southern Tibet and under Tarim basin. Low velocity under northern Tibet indicates hot and deformed mantle.

To test the resolution of the mid crust low velocity zones and the slow mantle velocity in northern Tibet in our model, we conduct a synthetic test. Our input model consists of a low velocity layer from 20 to 40 km inside the TP with velocity decrease of 5%. Low mantle velocity structure is confined in the northern Tibet with 5% velocity decrease than normal mantle. Crustal thickness within Tibet is 70 km while outside is 40 km. We use exactly the same ray paths as in real inversion for our test. The forward calculation is described in Sect. 3. Five second with a random noise added into the synthetic data as before. Figure 8 shows the three cross sections of input models and recovered models. Mid crust low velocity zones and mantle low velocity structure are generally well recovered in the cross sections. However, the Moho boundary between crust and mantle is smeared in the recovered images due to the limited vertical resolution of surface wave inversions.

Many previous tomographic studies of the TP and surrounding regions have been done with different data sets, coverage, and methods. Although our new model shows considerable improvement in resolution, the similarity in some of the major features suggests the robustness of the results. These features include fast mantle velocities in Sichuan, Qaidam, Tarim, and Junggar are reported by different studies (Huang et al. 2003; Liang et al. 2004; Huang and Zhao 2006; Obrebski et al. 2012), slow velocity anomalies in the mid-crust throughout most of the TP (Huang et al. 2003; Sun et al. 2010; Yang et al. 2012), and slow and fast velocity contrast in the upper mantle between north and south of Banggong-Nujiang suture (e.g., Owens

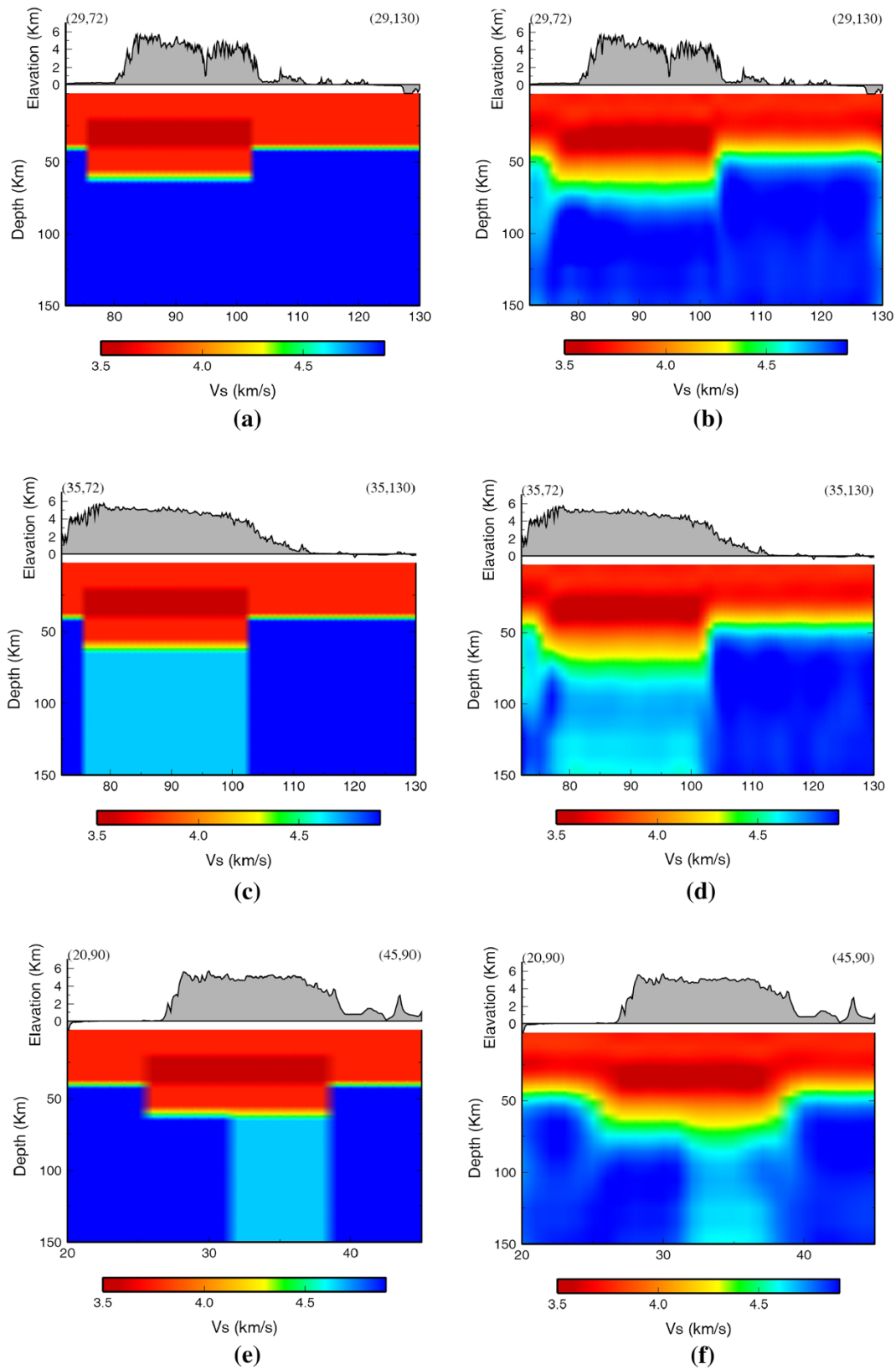


**Fig. 8** Synthetic test of mid crust low velocity zone and slow mantle velocity in the northern TP. Shown are three typical cross sections along 29° latitude in southern TP (*top*), 35° latitude in northern TP (*middle*), and 90° longitude across the TP (*bottom*). Cross sections of the input model are shown in the *left panels* (a, c, e). Corresponding recovered cross sections are shown in the *right* (b, d, f)

and Zandt 1997; Huang et al. 2003; Tilmann and Ni 2003; Liang and Song 2006). The cross sections and 100 s Rayleigh wave maps of Huang et al. (2003) revealed relative high velocity structures between 94° and 98°. This velocity anomaly coincides well with the fast velocity structure in our *S* velocity model. This structure difference between eastern and western Tibet is also observed in Pn velocities (Liang and Song 2006).

#### 4.3 North China Craton

The North China Craton (NCC) is another important area in our study with some large intraplate earthquakes in the recent history. NCC consists of the western (including Ordos Basin), and the eastern block, and the central region of mountains and rifts in between. The eastern NCC can be further divided into southern part and northern part (Bohai Basin). Geophysical observations suggest that the western block is stable while the eastern NCC has undergone rejuvenation with active geological processes. Cross section Fig. 6h passes through Ordos Basin, central NCC, Bohai Bay, and North Yellow Sea. Thick sediment deposition with slow velocity appears in basins (Ordos, Bohai). The western NCC shows thickened continent root and relative thicker crust while slow mantle velocity emerges under the central and eastern NCC. The thin crust and lithosphere in the eastern NCC along with elevated asthenosphere correlates with rifting, delamination, and upwelling in this region. The systematic change of velocity structure from west to east NCC in our model is consistent with many other surface wave tomographic studies (Huang et al. 2003, 2009; An et al. 2009; Zheng et al. 2011; Bao et al. 2013), Pn wave tomography (Liang et al. 2004), local and teleseismic P tomography (Tian et al. 2009; Xu and Zhao 2009), and receiver functions studies (e.g., Chen et al. 2008), which all suggest thinning of lithosphere and decrease in mantle velocity from west to east. The lithosphere thickness decreases from over 200 km in Ordos basin to as thin as 60 km in eastern NCC (Chen 2010).

The velocity contrast across Tanlu Fault suggests it may be a major fault and boundary cutting into the mantle lithosphere (Fig. 6h, i), which was suggested previously (Chen et al. 2006; An et al. 2009). The velocity is discontinuous across the Tanlu Fault with low velocity anomalies in the uppermost mantle beneath the fault. The east–west cross section in the south (Fig. 6i) passes through Yangze Craton, southern eastern NCC, and Southern Yellow sea, where the lithosphere under Yangze Craton is significantly thicker than under the southern part of the eastern NCC. Two north–south cross sections compare the velocity structure between western NCC (Fig. 6j) and eastern NCC (Fig. 6k). In the western cross section, thin

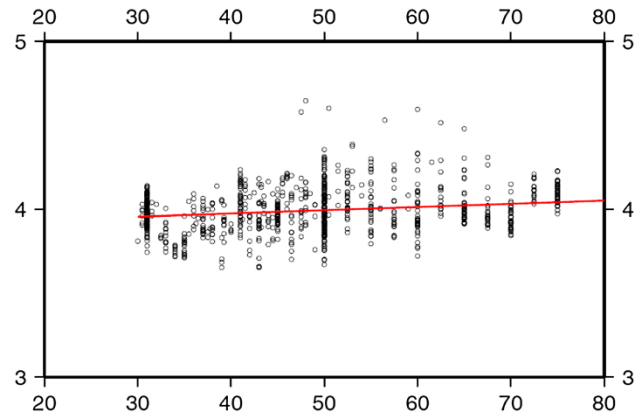


**Fig. 9** Calibration to find crustal thickness from our *S* model. Plotted is the depth of CRUST 2.0 Moho (*horizontal axis*) and the corresponding *S* velocity retrieved from our model. Each data point (*open circle*) corresponds to each grid in our model. *Red line* is the linear regression. Note the gentle slope of the *line*, indicating the Moho depth can be estimated using the nearly constant *S* velocity

mantle lithosphere under South China Fold Belt, thick continent root under Yangze Craton, and Ordos Basin are well imaged. While in the eastern cross section, the mantle lithosphere is significant thinner that reaches only about 75–100 km depth. The clear different in the mantle lithosphere between the western and eastern NCC, suggests that the eastern part and the Shanxi graben may be undergoing mantle transformation at the present time while the western part remains stable.

#### 4.4 Derived models

##### 4.4.1 Derived Moho map

The *S* velocity model we have obtained can be used to explore the model parameters and characteristics. Because of the apparent correlation of the *S* velocities and crustal thickness, one useful exercise is to derive a crustal thickness model based on the *V<sub>s</sub>* model. If we use the *V<sub>s</sub>* that corresponds to the depth of the Moho as defined by the reference model CRUST 2.0, we find that the average of the *S* velocities is nearly constant (at about 4.0 km/s with a slight positive trend as a function of crustal thickness) (Fig. 9). We thus use the *S* velocity to find the true Moho depth using the linear relationship as a calibration. Specifically, to find the Moho at any given point, we use the following steps: (1) find the reference Moho depth from CRUST 2.0 for that location, (2) find the reference *V<sub>s</sub>* from the linear trend, and (3) find the depth that corresponds to the reference *V<sub>s</sub>* (that is close to the CRUST 2.0 depth). The procedure ensures that the newly derived Moho map (Fig. 10a) is similar to the CRUST 2.0 (Fig. 10b) overall, but the new map shows a much detailed structure that corresponds to the variation in the *S* velocities.

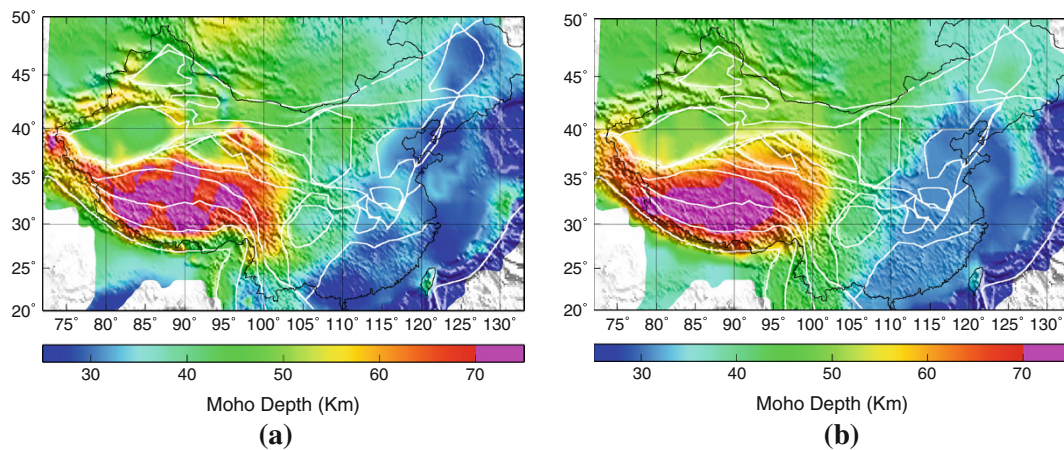


**Fig. 10** Map of crustal thickness derived from *S* velocity model (a), in comparison with CRUST 2.0 model (b)

#### 4.4.2 Average *S* model of the crust and upper mantle

The crustal thickness across the Chinese continent shows large variation, comparing average in upper, mid, and lower crust, as well as mantle is more meaningful than directly comparing velocities at the same depth. We thus construct averaged crustal and upper mantle models (Fig. 11a–d), based on the crustal thickness model that we have developed above. We divide the crust into three layers of equal thickness and define them as upper, mid, and lower crust, respectively.

Average upper crust velocity is very similar to velocity at 7.5 km (Fig. 5a), where low velocities are shown in the major basins, marginal seas and Himalaya front, while high velocities are found in South China fold belt. Average mid crust velocity model reveals low velocity layer throughout most of the TP. Eastern NCC and South China fold belt are also in low velocities. In contrast, Sichuan basin, Ordos basin, and South Yellow Sea show high velocity structure. Average lower crust velocity shows much smaller variation than that in the upper and mid crust. However, there shows a strong fast velocity anomaly in north western China, which is difficult to explain. This velocity anomaly also appears at 30 and 50 s group velocity maps with or without EGFs data (Fig. 7c–f). It is also imaged in *S* model by Sun et al. (2010) using ambient noise data only. It might be artifact due to relatively poor coverage in this area or some problematic data. However, since it is imaged from different data sets, this anomaly may indicate a real geological feature. Further investigation is needed to explore this issue in the future. Prominent features are seen in the average uppermost 80 km mantle, including high velocity in Tarim, Ordos, and Sichuan basins. The TP shows complicated structure with fast velocity in Indian plate and Lhasa block, as well as the velocity stripe along 95° while slow velocity appears in Songpan–Ganzi Fold Belt, western and northern Tibet. Although there is some detailed difference, our

mantle structure shows significant agreement with the Pn model derived from Liang and Song (2006). Low velocities are also shown in eastern NCC and South China Fold Belt as discussed in previous velocity maps and cross sections.

## 5 Summary

We presented a new *S*-tomography model (down to about 150 km) of China and surrounding regions, based surface (Rayleigh) wave dispersion measurements from a large amount of ambient noise and earthquake data. The combination of EGFs retrieved from ambient noise correlation and earthquake data increases the data coverage throughout the study region. We also derived new models for crustal thickness and averaged *S* velocities for upper, mid, and lower crust and the uppermost mantle. These results provide a fundamental data set for understanding continental dynamics and evolution. Below are some important features of the model.

- (1) Major basins are delineated with slow velocities at shallow depth, indicating thick sediment deposition. Major basins in the West (Tarim, Tulufan, Junggar, west Ordos, Sichua) as well as the Indian Shield show fast mantle lithosphere velocities, indicating strong, cold, and stable continental blocks. These strong blocks thus seem to play an important role in confining the deformation of the TP to be a triangular shape.
- (2) The mantle lithosphere of the northern Tibet has generally lower velocities than in the southern Tibet, correlating with the intrusion of the India lithosphere. However, there is significant *E–W* variation. The low velocity structure in the upper mantle under north and eastern TP correlates with surface geological

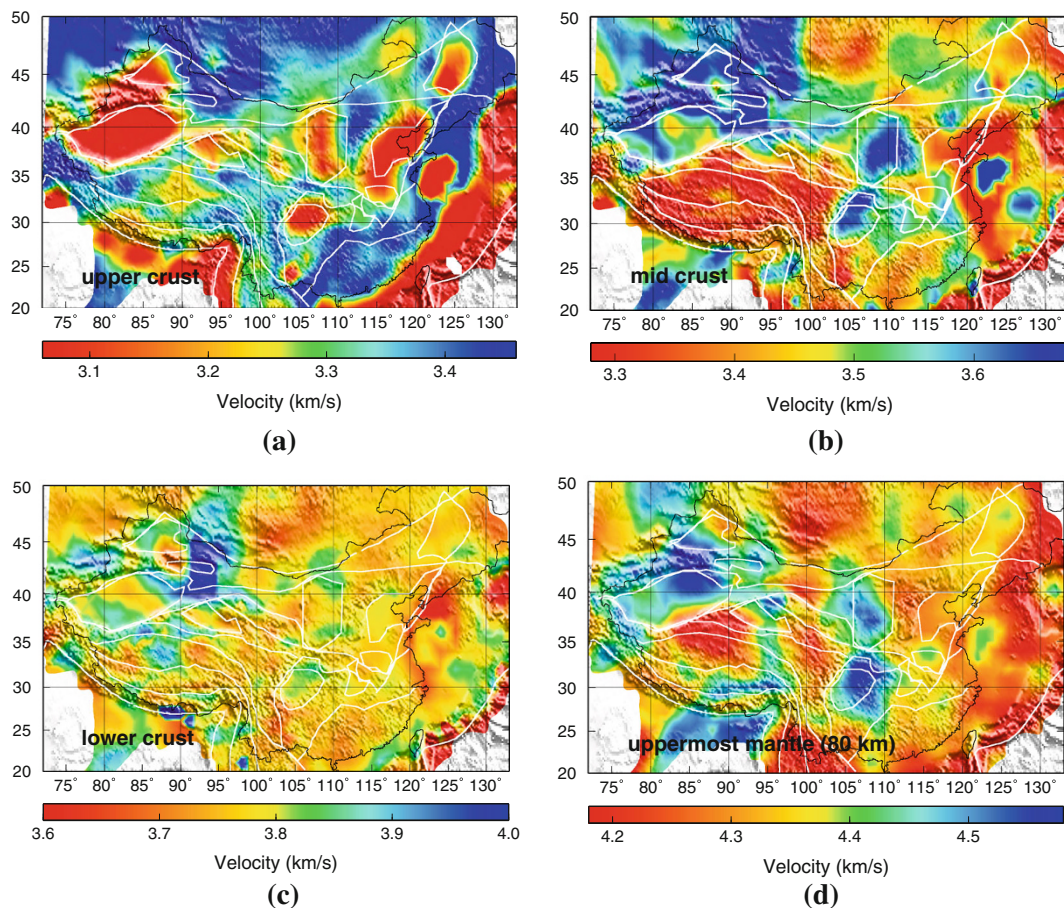


**Fig. 11** Derived average  $S$  velocity models for the upper crust (a), mid crust (b), lower crust (c), and uppermost 80 km of the mantle (d)

boundaries. A patch of high velocity anomaly is found under the eastern part of the TP, which may indicate intact mantle lithosphere. Widespread, prominent low-velocity zones are observed in mid-crust in much of the TP, suggesting a weak (and perhaps mobile) mid-crust.

- (3) Velocity contrast between eastern and western NCC is striking. The western NCC appears to be stable block with thick continental lithosphere root, while eastern NCC shows slow mantle velocities and thin lithosphere. The Tanlu Fault appears to be a major lithosphere boundary.

**Acknowledgments** The CNSN waveform data were provided by China Earthquake Network Center and the waveform data of the international stations and PASSCAL stations were from the IRIS Data Management Center. We thank detailed and constructive reviews from two anonymous reviewers. The figures were made using the GMT software (Wessel and Smith 1998). This work was partly supported by the Natural Science Foundation of China (41274056), the National Science Foundation of the United States (EAR-1215824), and Department of Geology, UIUC.

## References

- An MJ, Feng M, Zhao Y (2009) Destruction of lithosphere within the north China Craton inferred from surface wave tomography. *Geochem Geophys Geosyst* 10:Q08016. doi:[10.1029/2009GC002542](https://doi.org/10.1029/2009GC002542)
- Bao XW, Song XD, Xu MJ, Wang LS, Sun XX, Mi N, Yu D Y, Li H (2013) Crust and upper mantle structure of the North China Craton and the NE Tibetan Plateau and its tectonic implications. *Earth Planet Sci Lett*. doi:[10.1016/j.epsl.2013.03.015i](https://doi.org/10.1016/j.epsl.2013.03.015i)
- Bensen GD, Ritzwoller MH, Barmin MP, Levshin AL, Lin F, Moschetti MP, Shapiro NM, Yang Y (2007) Processing seismic ambient noise data to obtain reliable broad-band surface wave dispersion measurements. *Geophys J Int* 169(3):1239–1260
- Bensen GD, Ritzwoller MH, Shapiro NM (2008) Broadband ambient noise surface wave tomography across the United States. *J Geophys Res* 113:B05306. doi:[10.1029/2007JB005248](https://doi.org/10.1029/2007JB005248)
- Campillo M, Paul A (2003) Long-range correlations in the diffuse seismic coda. *Science* 299(5606):547–549
- Chen L (2010) Concordant structural variations from the surface to the base of the upper mantle in the North China Craton and its tectonic implications. *Lithosphere* 120:96–115. doi:[10.1016/j.lithos.2009.12.007](https://doi.org/10.1016/j.lithos.2009.12.007)
- Chen WP, Molnar P (1981) Constraints on the seismic wave velocity structure beneath the Tibetan Plateau and their tectonic implications. *J Geophys Res* 86:5937–5962

- Chen L, Zheng TY, Xu WW (2006) A thinned lithospheric image of the Tanlu Fault Zone, eastern China: constructed from wave equation based receiver function migration. *J Geophys Res* 111:B09312. doi:[10.1029/2005JB003974](https://doi.org/10.1029/2005JB003974)
- Chen L, Tao W, Zhao L, Zheng TY (2008) Distinct lateral variation of lithospheric thickness in the northeastern North China Craton. *Earth Planet Sci Lett* 267:56–68. doi:[10.1016/j.epsl.2007.11.024](https://doi.org/10.1016/j.epsl.2007.11.024)
- Chung SL, Lo CH, Lee TY, Zhang YQ, Xie YW, Li XH, Wang KL, Wang PL (1998) Diachronous uplift of the Tibetan plateau starting 40 Myr ago. *Nature* 394:769–773
- Herrmann RB (1991) Computer program in seismology. Surface wave inversion, vol IV. Department of Earth and Atmosphere Sciences, St. Louis University
- Holt WE, Wallace TC (1990) Crustal thickness and upper mantle velocities in the Tibetan plateau region from the inversion of regional Pnl waveforms: evidence for a thick upper mantle lid beneath southern Tibet. *J Geophys Res* 95:12499–12525
- Huang JL, Zhao DP (2006) High-resolution mantle tomography of China and surrounding regions. *J Geophys Res* 111:B09305
- Huang ZX, Su W, Peng YJ, Zheng YJ, Li HY (2003) Rayleigh wave tomography of China and adjacent regions. *J Geophys Res* 108:2073. doi:[10.1029/2001JB001696](https://doi.org/10.1029/2001JB001696)
- Huang ZX, Li HY, Zheng YJ, Peng YJ (2009) The lithosphere of North China Craton from surface wave tomography. *Earth Planet Sci Lett* 288:164–173
- Lees JM, Crosson RS (1989) Tomographic inversion for three-dimensional velocity structure at Mount St. Helens using earthquake data. *J Geophys Res* 94:5716–5728
- Levshin AL, Ritzwoller MH (2001) Automated detection, extraction, and measurement of regional surface waves. *Pure Appl Geophys* 158(8):1 531–1 545
- Li C, van der Hilst RD, Meltzer AS, Engdahl ER (2008) Subduction of the Indian lithosphere beneath the Tibetan Plateau and Burma. *Earth Planet Sci Lett* 274:157–168. doi:[10.1016/j.epsl.2008.07.016](https://doi.org/10.1016/j.epsl.2008.07.016)
- Liang CT, Song XD (2006) A low velocity belt beneath northern and eastern Tibetan Plateau from Pn tomography. *Geophys Res Lett* 33:L22306. doi:[10.1029/2006GL02792](https://doi.org/10.1029/2006GL02792)
- Liang CT, Song XD, Huang JL (2004) Tomographic inversion of Pn travel times in China. *J Geophys Res* 109:B11
- Lin FC, Moschetti MP, Ritzwoller MH (2008) Surface wave tomography of the western United States from ambient seismic noise: Rayleigh and Love wave phase velocity maps. *Geophys J Int* 173(1):281–298
- Obrebski M, Allen RM, Zhang FX, Pan JT, Wu QJ, Hung SH (2012) Shear wave tomography of China using joint inversion of body and surface wave constraints. *J Geophys Res* 117:B01311. doi:[10.1029/2011JB008349](https://doi.org/10.1029/2011JB008349)
- Owens TJ, Zandt G (1997) Implications of crustal property variations for models of Tibetan Plateau evolution. *Nature* 387:37–43
- Ritzwoller MH, Levshin AL, Ratnikova LI, Egorkin AA (1998) Intermediate-period group-velocity maps across Central Asia western China and parts of the Middle East. *Geophys J Int* 134(2):315–328
- Rodgers AJ, Schwartz SY (1998) Lithospheric structure of the Qiangtang Terrane, northern Tibetan Plateau, from complete regional waveform modeling: evidence for partial melt. *J Geophys Res* 103:7137–7152
- Sabra KG, Gerstoft P, Roux P, Kuperman WA, Fehler MC (2005) Surface wave tomography from microseisms in Southern California. *Geophys Res Lett* 32:L14311
- Shapiro NM, Campillo M (2004) Emergence of broadband Rayleigh waves from correlations of the ambient seismic noise. *Geophys Res Lett* 31(7):L07614
- Shapiro NM, Campillo M, Stehly L, Ritzwoller MH (2005) High-resolution surface-wave tomography from ambient seismic noise. *Science* 307(5715):1615–1618
- Sun XL, Song XD, Zheng SH, Yang YJ, Ritzwoller MH (2010) Three dimensional shear velocity structure of crust and upper mantle in China from ambient noise surface wave tomography. *Earthq Sci* 23:449–463
- Tian Y, Zhao DP, Sun RM, Teng JW (2009) Seismic imaging of the crust and upper mantle beneath the North China Craton. *Phys Earth Planet Interior* 172:169–182. doi:[10.1016/j.pepi.2008.09.002](https://doi.org/10.1016/j.pepi.2008.09.002)
- Tilmann F, Ni J (2003) Seismic imaging of the downwelling Indian lithosphere beneath central Tibet. *Science* 300(5624):1 424–1 427
- Weaver RL, Lobkis OI (2001) On the emergence of the Green's function in the correlations of a diffuse field. *J Acoust Soc Am* 110:3 011–3 017
- Weaver RL, Lobkis OI (2004) Diffuse fields in open systems and the emergence of the Green's function. *J Acoust Soc Am* 116:2 731–2 734
- Wessel P, Smith WHF (1998) New improved version of the generic mapping tools released. *EOS Trans AGU* 79:579
- Xu PF, Zhao DP (2009) Upper-mantle velocity structure beneath the North China Craton: implications for lithospheric thinning. *Geophys J Int* 177:1279–1283. doi:[10.1111/j.1365-246X.2009.04120.x](https://doi.org/10.1111/j.1365-246X.2009.04120.x)
- Xu Y, Liu F, Liu J, Chen H (2002) Crust and upper mantle structure beneath western China from P wave travel time tomography. *J Geophys Res* 107(B10):2220. doi:[10.1029/2001JB000402](https://doi.org/10.1029/2001JB000402)
- Yang Y, Ritzwoller MH, Levshin AL, Shampiro NM (2007) Ambient noise Rayleigh wave tomography across Europe. *Geophys J Int* 168(1):259–274
- Yang Y, Li A, Ritzwoller MH (2008) Crustal and uppermost mantle structure in southern Africa revealed from ambient noise and teleseismic tomography. *Geophys J Int* 174(1):235–248
- Yang YJ, Ritzwoller MH, Zheng Y, Shen WS, Levshin AL, Xie ZJ (2012) A synoptic view of the distribution and connectivity of the mid-crustal low velocity zone beneath Tibet. *J Geophys Res* 117. doi:[10.1029/2011JB008810](https://doi.org/10.1029/2011JB008810)
- Yao H, van der Hilst RD, de Hoop MV (2006) Surface wave array tomography in SE Tibet from ambient seismic noise and two-station analysis—I Phase velocity maps. *Geophys J Int* 166:732–744
- Yao H, Beghein C, van der Hilst RD (2008) Surface wave array tomography in SE Tibet from ambient seismic noise and two-station analysis-II. Crustal and upper-mantle structure. *Geophys J Int* 173(1):205–219
- Zheng SH, Sun XL, Song XD, Yang YJ, Ritzwoller MH (2008) Surface wave tomography of China from ambient seismic noise correlation. *Geochem Geophys Geosyst* 9:Q05020. doi:[10.1029/2008GC001981](https://doi.org/10.1029/2008GC001981)
- Zheng Y, Shen WS, Zhou LQ, Yang YJ, Xie ZJ, Ritzwoller MH (2011) Crust and uppermost mantle beneath the North China Craton, northeastern China, and the Sea of Japan from ambient noise tomography. *J Geophys Res*. doi:[10.1029/2011JB008637](https://doi.org/10.1029/2011JB008637)
- Zhou LQ, Xie JY, Shen WS, Zheng Y, Yang YJ, Shi HX, Ritzwoller MH (2012) The structure of the crust and uppermost mantle beneath South China from ambient noise and earthquake tomography. *Geophys J Int* 189:1565–1583. doi:[10.1111/j.1365-246X.2012.05423.x](https://doi.org/10.1111/j.1365-246X.2012.05423.x)